

Red-giant seismic properties analyzed with CoRoT[★]

B. Mosser¹, K. Belkacem^{2,1}, M.-J. Goupil¹, A. Miglio^{2,★★}, T. Morel², C. Barban¹, F. Baudin³, S. Hekker^{4,5},
R. Samadi¹, J. De Ridder⁵, W. Weiss⁶, M. Auvergne¹, and A. Baglin¹

¹ LESIA, CNRS, Université Pierre et Marie Curie, Université Denis Diderot, Observatoire de Paris, 92195 Meudon cedex, France
e-mail: benoit.mosser@obspm.fr

² Institut d'Astrophysique et de Géophysique, Université de Liège, Allée du 6 Août 17, 4000 Liège, Belgium

³ Institut d'Astrophysique Spatiale, UMR 8617, Université Paris XI, Bâtiment 121, 91405 Orsay Cedex, France

⁴ School of Physics and Astronomy, University of Birmingham, Edgbaston, Birmingham B15 2TT, UK

⁵ Instituut voor Sterrenkunde, K. U. Leuven, Celestijnenlaan 200D, 3001 Leuven, Belgium

⁶ Institut für Astronomie (IfA), Universität Wien, Türkenschanzstrasse 17, 1180 Wien, Austria

Received 11 January 2010 / Accepted 1 April 2010

ABSTRACT

Context. The CoRoT 5-month long observation runs provide us with the opportunity to analyze a large variety of red-giant stars and derive their fundamental parameters from their asteroseismic properties.

Aims. We perform an analysis of more than 4600 CoRoT light curves to extract as much information as possible. We take into account the characteristics of both the star sample and the method to ensure that our asteroseismic results are as unbiased as possible. We also study and compare the properties of red giants in two opposite regions of the Galaxy.

Methods. We analyze the time series using the envelope autocorrelation function to extract precise asteroseismic parameters with reliable error bars. We examine first the mean wide frequency separation of solar-like oscillations and the frequency of the maximum seismic amplitude, then the parameters of the excess power envelope. With the additional information of the effective temperature, we derive the stellar mass and radius.

Results. We identify more than 1800 red giants among the 4600 light curves and obtain accurate distributions of the stellar parameters for about 930 targets. We are able to reliably measure the mass and radius of several hundred red giants. We derive precise information about the stellar population distribution and the red clump. By comparing the stars observed in two different fields, we find that the stellar asteroseismic properties are globally similar, but that the characteristics are different for red-clump stars.

Conclusions. This study demonstrates the efficiency of statistical asteroseismology: validating scaling relations allows us to infer fundamental stellar parameters, derive precise information about red-giant evolution and interior structure, analyze and compare stellar populations from different fields.

Key words. stars: fundamental parameters – stars: interiors – stars: evolution – stars: oscillations – stars: abundances

1. Introduction

The high-precision, continuous, long photometric time series recorded by the CoRoT satellite allow us to study a large number of red giants. In a first analysis of CoRoT red giants, [De Ridder et al. \(2009\)](#) reported the presence of radial and non-radial oscillations in more than 300 giants. [Hekker et al. \(2009\)](#), after a careful analysis of about 1000 time series, demonstrated that there is a tight relation between the large separation and the frequency of maximum oscillation amplitude. [Miglio et al. \(2009\)](#) identified the signature of the red clump, which agrees with synthetic populations. [Kallinger et al. \(2010\)](#) exploited the possibility of measuring stellar mass and radius from the asteroseismic measurements, even when the stellar luminosity and effective temperature are not accurately known.

In this paper, we focus specifically on the statistical analysis of a large set of stars in two different fields observed with CoRoT ([Auvergne et al. 2009](#)). One is located towards the Galactic

center (LRc01), the other in the opposite direction (LRa01). We first derive precise asteroseismic parameters, and then stellar parameters. We also examine how these parameters vary with the frequency ν_{\max} of the maximum amplitude. The new analysis that we present in this paper was made possible by the use of the autocorrelation method ([Mosser & Appourchaux 2009](#)), which significantly differs from those used in other works ([Mathur et al. 2010b](#); [Hekker et al. 2009](#); [Huber et al. 2009](#)). It does not rely on the identification of the excess oscillation power, but on the direct measurement of the acoustic radius τ of a star. This acoustic radius is related to the large separation commonly used in asteroseismology ($\Delta\nu = 1/2\tau$). The chronometer is provided by the autocorrelation of the asteroseismic time series, which is sensitive to the travel time of a pressure wave crossing the stellar diameter twice, i.e., 4 times the acoustic radius. The calculation of this autocorrelation as the Fourier spectrum of the Fourier spectrum with the use of narrow window for a local analysis in frequency was proposed by [Roxburgh & Vorontsov \(2006\)](#). [Mosser & Appourchaux \(2009\)](#) formalized and quantified the performance of the method based on the envelope autocorrelation function (EACF).

By applying this method and its related automated pipeline, we search for the signature of the mean large separation of a solar-like oscillating signal in the autocorrelation of the time

[★] The CoRoT space mission, launched on 2006 December 27, was developed and is operated by the CNES, with participation of the Science Programs of ESA, ESAs RSSD, Austria, Belgium, Brazil, Germany and Spain.

^{★★} Postdoctoral Researcher, Fonds de la Recherche Scientifique – FNRS, Belgium.

series. Mosser & Appourchaux (2009) illustrated how to deal with the noise contribution entering the autocorrelation function, which enabled them to determine the reliability of the large separations obtained with this method. Basically, they scaled the autocorrelation function on the basis of the noise contribution. With this scaling, they demonstrated how to define the threshold level above which solar-like oscillations are detected and how a reliable large separation can be derived.

An appreciable advantage of the method is that the large separation is determined first, without any assumptions or any fit to the background. As a consequence, the method directly focuses on the key parameters of asteroseismic observations: the mean value $\langle\Delta\nu\rangle$ of the large separation and the frequency ν_{\max} at which the oscillation signal reaches a maximum. Since the method does not rely on the detection of an energy excess, it can operate at low signal-to-noise ratio (SNR), as shown by Mosser et al. (2009). The value of the frequency ν_{\max} , derived first from the maximum autocorrelation signal, is then inferred from the maximum excess power observed in a smoothed Fourier spectrum corrected for the background component. The different steps of the pipeline for the automated analysis of the time series are presented in Mosser & Appourchaux (2010).

The method has been tested on CoRoT main-sequence stars (Benomar et al. 2009; Barban et al. 2009; García et al. 2009; Deheuvels et al. 2010; Mathur et al. 2010a) and proven its ability to derive reliable results efficiently from low SNR light curves, when other methods fail or derive questionable results (Mosser et al. 2009; Gaulme et al. 2010). The method also allowed the correct identification of the degree of the eigenmodes of the first CoRoT target HD 49933 (Mosser et al. 2005; Appourchaux et al. 2008; Mosser & Appourchaux 2009). The EACF method and its automated pipeline were tested on the CoRoT red giants presented by De Ridder et al. (2009) and Hekker et al. (2009), and also on the Kepler red giants (Stello et al. 2010; Bedding et al. 2010).

The paper is organized as follows. In Sect. 2, we present the analysis of the CoRoT red giants using the EACF and define the way the various seismic parameters are derived. We also determine the frequency interval where we can extract unbiased global information. Measurements of the asteroseismic parameters $\langle\Delta\nu\rangle$ and ν_{\max} are presented in Sect. 3 and compared to previous studies. We also present the variation $\Delta\nu(\nu)$ performed with the EACF. Section 4 deals with the parameters related to the envelope of the excess power observed in the Fourier spectra, for which we propose scaling laws. From the asteroseismic parameters ν_{\max} and $\langle\Delta\nu\rangle$, we determine the red-giant mass and radius in Sect. 5. Compared to Kallinger et al. (2010), we benefit from the stellar effective temperatures obtained from independent photometric measurements, so that we do not need to refer to stellar modeling to derive the fundamental parameters. We then specifically address the properties of the red clump in Sect. 6, so that we can carry out a quantitative comparison with the synthetic population performed by Miglio et al. (2009). The difference between the red-giant populations observed in 2 different fields of view is also presented in Sect. 6. Section 7 is devoted to discussions and conclusions.

2. Data

2.1. Time series

Our results are based on time series recorded during the first long CoRoT runs in the direction of the Galactic center (LRc01) and in the opposite direction (LRa01). These long runs lasted

Table 1. Red-giant targets.

Run	T (d)	N_0	N_1	N_2	N_3
LRc01	142 d	9938	3388	1399	710
LRa01	128 d	2826	1271	428	219
total	–	12764	4659	1827	929
ratio (%)	–	–	100%	39%	20%

Notes. Among N_0 targets a priori identified as red giants in the input catalog of each field, N_1 light curves were available and analyzed in each run. Among these, N_2 targets show solar-like oscillation patterns for which we can derive precise values of $\langle\Delta\nu\rangle$ and ν_{\max} . Envelope parameters can be precisely determined for N_3 targets.

approximately 140 days, providing us with a frequency resolution of about $0.08 \mu\text{Hz}$. Red giants were identified according to their location in a color–magnitude diagram with $J - K$ in the range $[0.6, 1.0]$ and K brighter than 12.

In Table 1, we present the number of targets that were considered. We indicate as N_0 the number of red giants identified in each field according to a color–magnitude criterion, only a fraction of which were effectively observed. We indicate as N_1 the number of time series available, hence analyzed. Among the N_1 time series, N_2 targets exhibit reliable solar-like oscillations for which we can derive precise values of $\langle\Delta\nu\rangle$ and ν_{\max} . We remark that the ratio N_2/N_1 is high: a large fraction of the stars identified as red-giant candidates exhibit solar-like oscillations.

2.2. Data analysis

As explained by Mosser & Appourchaux (2010), the measurement of the mean value $\langle\Delta\nu\rangle$ of the large separation presupposes scaling relations between this parameter, the frequency of maximum seismic amplitude ν_{\max} , and the full-width at half-maximum of the excess power envelope $\delta\nu_{\text{env}}$. These scaling relations are used to search for the optimized asteroseismic signature. The threshold level for a positive detection of solar-like oscillations and the quality of the signature are given by the maximum \mathcal{F} reached by the EACF (Sect. 3.3 of Mosser & Appourchaux 2009). The method is able to automatically exclude unreliable results and calculate error bars *without any comparison to theoretical models*.

For stars with low SNR seismic time series, only $\langle\Delta\nu\rangle$ and ν_{\max} can be reliably estimated. At higher SNR, we can also derive the parameters of the envelope corresponding to the oscillation energy excess. This envelope is supposed to be Gaussian, centered on ν_{\max} , with a full-width at half-maximum $\delta\nu_{\text{env}}$. We also measure the height-to-background ratio \mathcal{H}/\mathcal{B} in the power spectral density smoothed with a $\langle\Delta\nu\rangle$ -broad cosine filter given by the ratio of the excess power height \mathcal{H} to the activity background \mathcal{B} . The determination of these envelope parameters requires a high enough height-to-background ratio (≥ 0.2). Finally, the maximum amplitude of the modes and the FWHM of the envelope were precisely determined for N_3 targets, for which precise measurements of the stellar mass and radius can then be derived.

Thanks to the length of the runs and the long-term stability of CoRoT, large separations below $1 \mu\text{Hz}$ have been measured for the first time. This represents about 10 times the frequency resolution of $0.08 \mu\text{Hz}$. We emphasize that the method based on the EACF allows us to obtain a higher resolution since the achieved precision is related to the ratio of the time series sampling to the acoustic radius (see Eq. (A.8) of Mosser & Appourchaux 2009). We can reach a frequency resolution of about 3% when

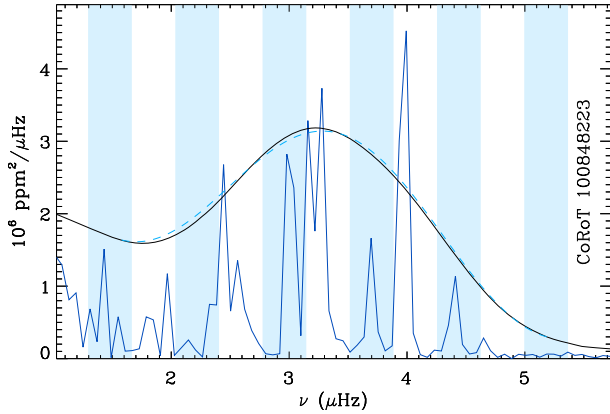


Fig. 1. Fourier spectrum of a target with a very low mean value of the large separation ($\langle \Delta \nu \rangle = 0.74 \mu\text{Hz}$, centered at $\nu_{\text{max}} = 3.45 \mu\text{Hz}$). The colored vertical ranges have a width equal to half the large separation. This spectrum exhibits a clear Tassoul-like pattern: modes of degree 0 and 2 are located in the uncolored regions whereas $\ell = 1$ modes are in the blue regions. For clarity, the amplitude of the envelope (black line) has been multiplied by 3. The dashed line represents the Gaussian fit to the excess power envelope, also multiplied by 3, superimposed on the background.

the excess power envelope is reduced to 3 times the large separation. Figure 1 gives an example of the fits obtained at low frequency. The CoRoT star 100848223 has a mean large separation $\langle \Delta \nu \rangle = 0.74 \pm 0.02 \mu\text{Hz}$ and a maximum oscillation frequency $\nu_{\text{max}} = 3.45 \pm 0.22 \mu\text{Hz}$.

2.3. Bias and error bars

The distribution of the targets can be biased by different effects that have to be carefully examined before extracting any statistical properties. Since we aim to relate global properties to ν_{max} , we examined how the distribution of red giants can be biased as a function of this frequency. We chose to consider only targets with ν_{max} below $100 \mu\text{Hz}$. For values above that level, the oscillation pattern can be severely affected by the orbit, at frequencies mixing the orbital and diurnal signatures ($161.7 \pm k 11.6 \mu\text{Hz}$, with k an integer). This high-frequency domain will be more easily studied with Kepler (Bedding et al. 2010).

On the other hand, brighter stars with larger radii, hence a low mean density, exhibit an oscillation pattern at very low frequency. In that respect, even if CoRoT has provided the longest continuous runs ever observed, these brighter targets that should be more likely to be observed are affected by the finite extent of the time series. The EACF allows us to examine the bias in the data, via the distribution of the autocorrelation signal as a function of frequency.

According to Mosser & Appourchaux (2009), the EACF amplitude \mathcal{F} scales as $(\mathcal{H}/\mathcal{B})^{1.5} \delta \nu_{\text{env}}$. This factor \mathcal{F} measures the quality of the data, since the relative precision of the measurement of $\langle \Delta \nu \rangle$ and ν_{max} varies as \mathcal{F}^{-1} . In contrast to the linear dependence with $\delta \nu_{\text{env}}$, which was theoretically justified by Mosser & Appourchaux (2009), the variation in \mathcal{F} with \mathcal{H}/\mathcal{B} was empirically derived from a fit based on main-sequence stars. We verified that this relation for the variation in \mathcal{F} with \mathcal{H}/\mathcal{B} cannot be extrapolated to red giants. The reason seems to be related to the difference between the oscillation patterns of red giants compared to main-sequence stars (Dupret et al. 2009). For $\nu_{\text{max}} \leq 80 \mu\text{Hz}$, the number of targets exhibiting solar-like

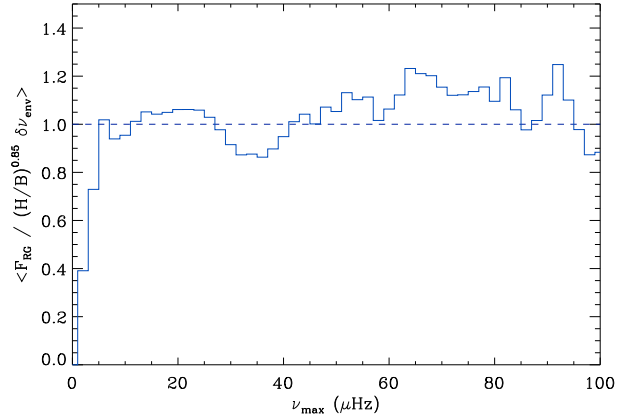


Fig. 2. Estimation of the bias, calculated from the mean ratio $\mathcal{F}_{\text{RG}}/(\mathcal{H}/\mathcal{B})^{0.85} \delta \nu_{\text{env}}$, as a function of the frequency of maximum amplitude ν_{max} .

oscillations is high enough to derive the exponent for giants, close to 0.85

$$\mathcal{F}_{\text{RG}} \propto \left(\frac{\mathcal{H}}{\mathcal{B}} \right)^{0.85} \delta \nu_{\text{env}}. \quad (1)$$

Owing to the very large number of red giants and the large variety of the targets, the distribution of the ratio $\mathcal{F}_{\text{RG}}/(\mathcal{H}/\mathcal{B})^{0.85} \delta \nu_{\text{env}}$ is broadened compared to the few solar-like stars considered in Mosser & Appourchaux (2009). Its mean value shows a clear decrease at frequencies below $6 \mu\text{Hz}$ and a plateau at higher frequency (Fig. 2). This can be interpreted as a deficit of high signal-to-noise data when $\nu_{\text{max}} < 6 \mu\text{Hz}$, hence a signature of a bias against low ν_{max} values. Above $80 \mu\text{Hz}$, the number of targets is small and these targets exhibit high EACF but low \mathcal{H}/\mathcal{B} ratio; however, the fit presented in Eq. (1) remains valid. The observed decrease in the number of targets with increasing ν_{max} is however coherent with the extrapolation from lower values, the observations of Hekker et al. (2009), and Kepler data (Bedding et al. 2010).

We conclude from this test that the distribution of the targets is satisfactorily sampled in the frequency range $[3.5, 100 \mu\text{Hz}]$, no bias being introduced by the method above $6 \mu\text{Hz}$ and especially in the most-populated area in the range $[30, 40 \mu\text{Hz}]$ corresponding to the red-clump stars (Girardi 1999; Miglio et al. 2009).

3. Frequency properties

3.1. Mean large separation and frequency of maximum amplitude

The mean large separation and the frequency of maximum amplitude have the most precise determination. The median values of the $1-\sigma$ uncertainties on $\langle \Delta \nu \rangle$ and ν_{max} are, respectively, about 0.6 and 2.4%. The scaling between ν_{max} and $\langle \Delta \nu \rangle$ reported by Hekker et al. (2009) for red giants and discussed by Stello et al. (2009) has been explored down to $\nu_{\text{max}} = 3.5 \mu\text{Hz}$ (or $\langle \Delta \nu \rangle = 0.75 \mu\text{Hz}$). We obtain a more precise determination of the scaling (Fig. 3), with more than 1300 points entering the fit, given by

$$\langle \Delta \nu \rangle \simeq (0.280 \pm 0.008) \nu_{\text{max}}^{0.747 \pm 0.003}, \quad (2)$$

where $\langle \Delta \nu \rangle$ and ν_{max} are in μHz . The $1-\sigma$ errors given in Eq. (2) are internal errors and cannot be considered as significant. We

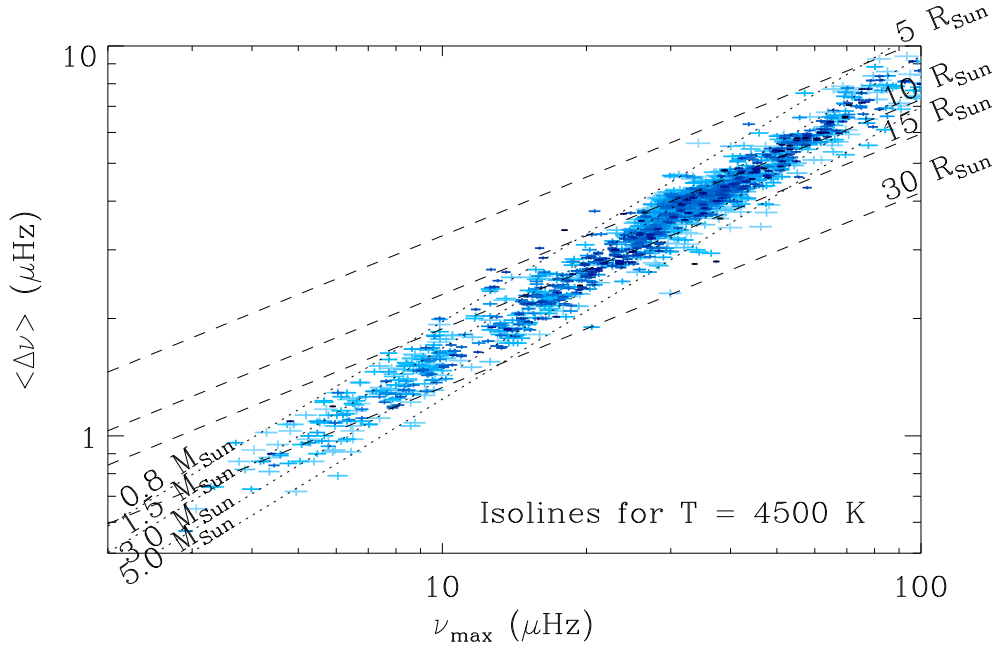


Fig. 3. $\nu_{\max} - \langle \Delta \nu \rangle$ relation for red-giant stars in LRA01 and LRC01, with all data satisfying a rejection of the null hypothesis at the 1% level. Isoradius and isomass lines, derived from the scaling given by Eqs. (9) and (10), are given for a mean effective temperature of 4500 K. Error bars in ν_{\max} and $\langle \Delta \nu \rangle$ are derived from the amplitude \mathcal{F} of the EACF. The color code allocates a darker color for measurements with high \mathcal{F} .

note that a modification of the data sample, for instance by reducing the frequency interval or the number of data, yields variations greater than the internal error bars. Hence, a more realistic relation with conservative error bars is

$$\langle \Delta \nu \rangle \simeq (0.280 \pm 0.02) \nu_{\max}^{0.75 \pm 0.01}, \quad (3)$$

with error bars that encompass the dispersion in the different sub-samples. The exponent differs from the value 0.784 ± 0.003 found in Hekker et al. (2009). Compared to this work, we consider a significantly larger data set with lower error bars and we do not scale the relation to the solar values of ν_{\max} and $\langle \Delta \nu \rangle$: this may explain the apparent discrepancy. We note that the exponent also differs from Stello et al. (2009), who found 0.772 ± 0.005 . This difference is not surprising since their fit is not based on red giants only but also includes main-sequence stars. Since the physical law explaining the relation between $\langle \Delta \nu \rangle$ and ν_{\max} is not fully understood, one cannot exclude that the different properties of the interior structure between giants and dwarfs may explain the difference; we discuss this point in more detail below (Sect. 5). On the other hand, the independent fits based on the data in LRC01 and LRA01 analyzed separately give convergent results, with exponent equal to 0.745 and 0.751, respectively.

The N_2 stars presented in Fig. 3 were selected with a \mathcal{F} factor greater than the threshold level 8 defined in Mosser & Appourchaux (2009). We verified that the 1- σ spread of the data around the fit given by Eq. (3) is low, about 9%. As illustrated by the isomass lines superimposed on the plot, derived from the estimates presented in Sect. 5, we note that the spread in the observed relation between $\langle \Delta \nu \rangle$ and ν_{\max} is mainly related to stellar mass. The metallicity dependence may also contribute to the spread; examining this effect is beyond the scope of this paper.

We examined the few cases that differ from the fit by more than 20%. As indicated in Miglio et al. (2009), they may correspond to a few halo stars (with large separation slightly above the main ridge of Fig. 3) or to higher mass stars (with large separation below the main ridge). We are confident that the possible targets with misidentified parameters in Fig. 3 do significantly

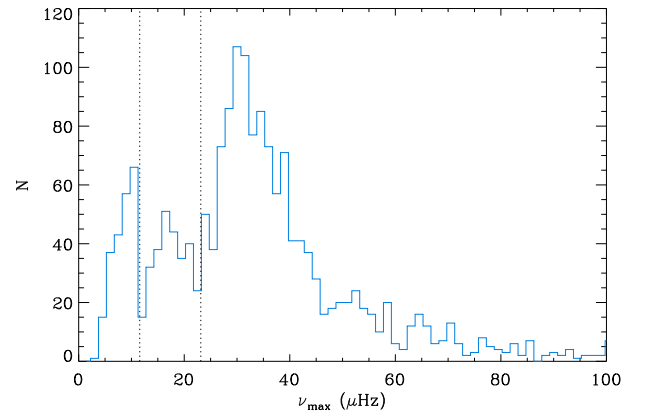


Fig. 4. Histogram of ν_{\max} with the signature of the red clump in the range [30, 40 μHz], with a major contribution at 30 and a shoulder plus a secondary bump just below 40 μHz . The deficits around 11.6 and 23.2 μHz (vertical dotted lines) are artifacts due to the low-Earth orbit of CoRoT.

influence neither the distributions nor the fit. The analysis presented below, that provides a seismic measure of the stellar mass and radius, allows us to exclude outliers with unrealistic stellar parameters, which are fewer than 2%.

Histograms of the distribution of the seismic parameters ν_{\max} and $\langle \Delta \nu \rangle$ have been plotted in Figs. 4 and 5. Deficits in the ν_{\max} distribution around the diurnal frequencies of 11.6 and 23.2 μHz are related to corrections motivated by the spurious excess power introduced by the CoRoT orbit. Since these artifacts have no fixed signature in $\langle \Delta \nu \rangle$, they are spread out, hence not perceptible, in the $\langle \Delta \nu \rangle$ distribution. The red-clump signature is easily identified as the narrow peak in the distribution of the mean large separation, around 4 μHz . The peak of the distribution of the maximum amplitude frequency is broader, with a maximum at 30 μHz and a shoulder around 40 μHz . This is in agreement with the synthetic population distribution (Girardi 1999; Miglio et al. 2009).

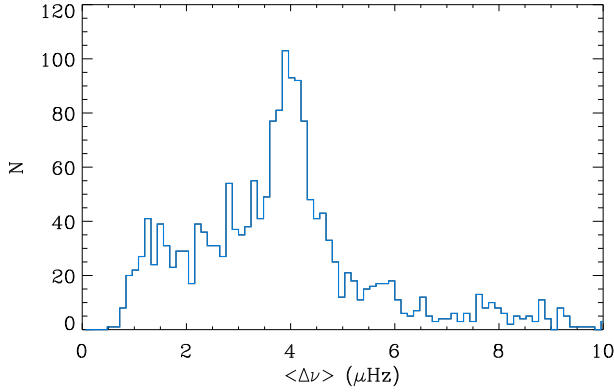


Fig. 5. Histogram of $\langle \Delta\nu \rangle$, with the red clump signature around 4 μHz .

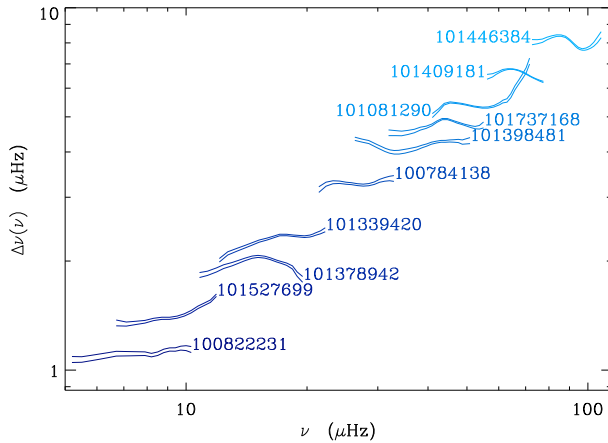


Fig. 6. $\Delta\nu(\nu)$ relation for a set of red giants with a mass derived from the seismic parameters in the range $[1.3, 1.4 M_{\odot}]$. Each pair of curves corresponds to a given red giant and gives the $1\text{-}\sigma$ error bar. The numbers correspond to the identifications in the CoRoT data base.

3.2. Variation in the large separation with frequency

The EACF allows us to examine the variation with frequency in the large separation ($\Delta\nu(\nu)$) and to derive more information about the stellar interior structure than given by the mean value. Significant variation in $\Delta\nu(\nu)$ is known to occur in the presence of rapid variation in either the density, the sound-speed, or the adiabatic exponent Γ_1 , or all three.

We selected targets with similar mass, in the range $[1.3, 1.4 M_{\odot}]$, as inferred from the relation discussed in Sect. 5, but for increasing values of ν_{max} . The corresponding $\Delta\nu(\nu)$ as a function of ν_{max} is plotted in Fig. 6. This allows us to examine how the global seismic signature evolves with stellar evolution. We note that the large separation $\Delta\nu(\nu)$ exhibits a significant modulation or gradient for nearly all of these stars. This variation in the large separation with frequency increases the uncertainty in the determination of $\langle \Delta\nu \rangle$ and the dispersion of the results. However, except for a few stars where the asymptotic pattern seems highly perturbed, we confirmed that the measurement of $\langle \Delta\nu \rangle$ provides a reliable indication of the mean value of $\Delta\nu(\nu)$ over the frequency range where excess power is detected. The statistical analysis of $\Delta\nu(\nu)$ is beyond the scope of this paper and will be carried out in future work.

Mosser & Appourchaux (2009) demonstrated that the analysis of $\Delta\nu(\nu)$ at high frequency resolution enables the identification of the mode degree in main-sequence stars observed with a sufficiently high enough SNR. This however seems ineffective for red giants, because the oscillation pattern observed in red

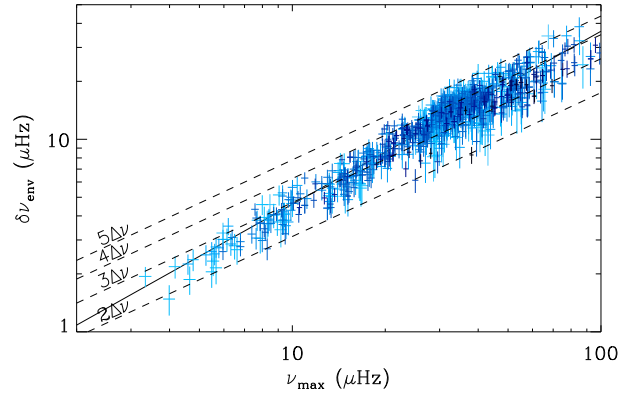


Fig. 7. $\nu_{\text{max}} - \delta\nu_{\text{env}}$ relation, with the same color code as Fig. 3. The solid line corresponds to the fit. The correspondence in units of the large separation is given by the dashed lines, which are guidelines for translating the excess power envelope width into large separation units.

giants (Carrier et al. 2010) differs from the pattern observed for subgiant and dwarf stars.

4. Oscillation excess power

We analyze the statistical properties of the parameters defining the excess power. They were measured for N_3 targets with the highest signal-to-noise ratio, the excess power envelope being derived from a smoothed power spectrum.

4.1. Excess power envelope

The full-width at half-maximum of the excess power envelope, plotted as a function of ν_{max} in Fig. 7, can be related to ν_{max} by

$$\delta\nu_{\text{env}} \simeq (0.59 \pm 0.02) \nu_{\text{max}}^{0.90 \pm 0.01}, \quad (4)$$

where ν_{max} is in μHz . As in Eq. (3) and for the same reason, we report only conservative error bars, of about two times the error bars in ν_{max} . Combining Eqs. (3) and (4), we can derive the ratio of the envelope width to the mean large separation

$$\frac{\delta\nu_{\text{env}}}{\langle \Delta\nu \rangle} \simeq (2.08 \pm 0.01) \nu_{\text{max}}^{0.15 \pm 0.02}, \quad (5)$$

where ν_{max} is in μHz . This ratio is closely related to the number of observable peaks. Owing to the small exponent, it does not vary significantly with ν_{max} . However, we remark that the envelope width is narrower than $3 \langle \Delta\nu \rangle$ when $\nu_{\text{max}} < 10 \mu\text{Hz}$. Extending the validity of this relation to solar-like stars does not seem possible, since the envelope width represents approximately $3.5 \langle \Delta\nu \rangle$ for a red giant in the red clump but $10 \langle \Delta\nu \rangle$ for a main-sequence star (Mosser & Appourchaux 2009). A major modification of the multiplicative parameter and/or of the exponent of the scaling law may occur as the stellar class changes.

Measurements at frequencies above $100 \mu\text{Hz}$ will help us to establish the exact relation for $\delta\nu_{\text{env}}(\nu_{\text{max}})$. We noted that the measurement of the envelope width is sensitive to the method, to the low-pass filter applied to the spectrum, if any, and to the estimate of the background. Since smoothing or averaging with a large filter width is inadequate for red giants with narrow excess power envelopes, and since an inadequate estimate of the background immediately translates into a biased determination of $\delta\nu_{\text{env}}$, we used a narrow smoothing, about $1.5 \langle \Delta\nu \rangle$.

We also directly estimated the number of eigenmodes with an H0 test (Appourchaux 2004). Data were rebinned over 5 pixels. Selected peaks were empirically identified to the same mode

Table 2. Number of detected peaks.

ν range (μHz)	\bar{n}_{\min}	\bar{n}_{\max}	\bar{N}_{peak}
≤ 15	4.1	9.8	8
15 – 20	5.0	11.0	8
20 – 30	5.5	11.3	7
30 – 40	6.1	11.9	7
40 – 60	7.0	13.1	7
60 – 100	8.3	15.1	7
100 – 300	8.9	15.9	8

Notes. For each frequency interval, \bar{n}_{\min} and \bar{n}_{\max} are the median values of the minimum and maximum detected eigenfrequencies expressed in unit $\langle\Delta\nu\rangle$; \bar{N}_{peak} is the median of the number of detected peaks, at a rejection level of 10%.

if their separation in frequency is smaller than $\langle\Delta\nu\rangle/30$. The median number \bar{N}_{peak} of peaks detected as a function of frequency is given in Table 2. We note that this number does not vary along the spectrum, in agreement with the small exponent of Eq. (5).

Estimates of the minimum and maximum orders of the detected peaks were simply obtained by dividing the minimum and maximum eigenfrequencies selected with the H0 test by $\langle\Delta\nu\rangle$. They vary in agreement with the exponent given by Eq. (5) (Table 2).

4.2. Temperature

Information about effective temperature is required to relate the oscillation amplitude to interior structure parameters. Effective temperatures were derived from dereddened 2MASS color indices using the calibrations of Alonso et al. (1999), as described in Baudin et al. (2010), for stars in LRC01. For the 3 stars without 2MASS data, optical $BVr'i'$ magnitudes taken from Exo-Dat were used (Deleuil et al. 2009). We adopted $A_V = 0.6$ mag for LRA01 based on the extinction maps of Dobashi et al. (2005) and Rowles & Froebrich (2009). As for LRC01, the good agreement between the T_{eff} values derived from near-IR and optical data indicates that this estimate is appropriate. The statistical uncertainty in these temperatures is about 150 K considering the internal errors in the calibrations and typical uncertainties in the photometric data, reddening, and metallicity. In terms of the systematic uncertainties, employing other calibrations would have resulted with temperature differences smaller than 150 K (Alonso et al. 1999).

A clear correlation between T_{eff} and ν_{\max} is given by

$$T \propto \nu_{\max}^{0.04 \pm 0.01}. \quad (6)$$

4.3. Amplitude

Maximum amplitudes of radial modes were computed according to the method proposed by Michel et al. (2009) for CoRoT photometric measurement. The distribution of the maximum mode amplitude as a function of ν_{\max} , presented in Fig. 8, is

$$A_{\max} \simeq (1550 \pm 100) \nu_{\max}^{-0.85 \pm 0.02} \quad (7)$$

where A_{\max} is in parts-per-million (ppm) and again ν_{\max} is in μHz . The median relative dispersion is about 50%. The fits based on LRC01 and LRA01 data separately are again equivalent. To avoid biasing the exponent with data exhibiting a gradient in signal-to-noise ratio with frequency, we estimated the exponents for subsets of stars with similar signal-to-noise ratios. This

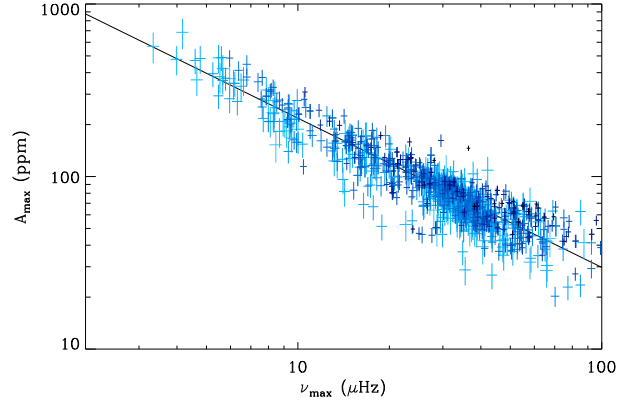


Fig. 8. $\nu_{\max} - A_{\max}$ relation. Same color code as Fig. 3. The solid line indicates the best fit.

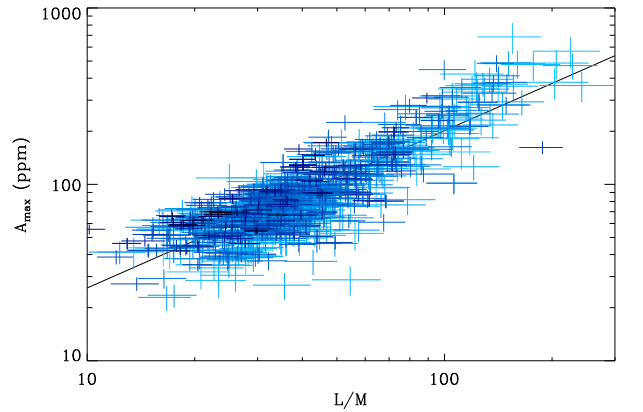


Fig. 9. $A_{\max} - L/M$ relation. The fit assumes all T_{eff} to be equal to the mean value. Same color code as in Fig. 3.

proves to be efficient since we then obtain convergent results for the exponent in Eq. (7).

Using several 3D simulations of the surface of main-sequence stars, Samadi et al. (2007) have found that the maximum of the mode amplitude in *velocity* scales as $(L/M)^s$ with $s = 0.7$. This scaling law reproduces rather well the main-sequence stars observed in Doppler velocity. When extrapolated to the red-giant domain ($L/M \geq 10$), this scaling law illustrates a good agreement with the giant and subgiant stars observed in Doppler velocity. To derive the mode amplitude in terms of bolometric intensity fluctuations from the mode amplitude in velocity, one usually assumes the adiabatic relation proposed by Kjeldsen & Bedding (1995). For the mode amplitudes in intensity, this gives a scaling law of the form $(L/M)^s T_{\text{eff}}^{-1/2}$, which requires the measurement of effective temperatures. Because of the Stefan-Boltzmann law, L/M scales as T_{eff}^4/g , hence as $T_{\text{eff}}^{7/2}/\nu_{\max}$.

As a consequence of Eq. (6), $T_{\text{eff}}^{7/2}/\nu_{\max}$ does not scale exactly as ν_{\max}^{-1} . We then obtain the scaling of the amplitude with $(L/M)^s T_{\text{eff}}^{-1/2}$ (Fig. 9)

$$A_{\max} \propto \left(\frac{L}{M}\right)^{0.89 \pm 0.02} T_{\text{eff}}^{-1/2}. \quad (8)$$

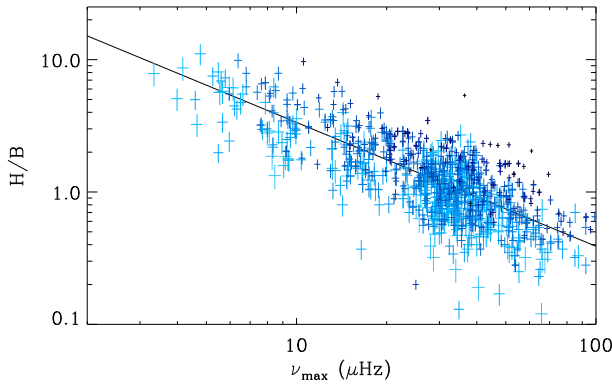
The spread around the global fit is as large as for the relation $A_{\max}(\nu_{\max})$ (Eq. 8). The influence of T_{eff} in Eq. (8) gives an exponent s that differs from the opposite of the exponent in Eq. (7) as would be the case if all temperatures were fixed to a single mean value. Finally, we derive an exponent of the scaling law between the maximum amplitude and the ratio L/M , 0.89 ± 0.02 , which

Table 3. Calibration of the red-giant mass and radius.

star	T_{eff} (K)	ν_{max}(μHz).....	$\langle\Delta\nu\rangle$	R_{mod} R_{\odot}	R	M_{mod} M_{\odot}	M	Ref.
HD 181907	4760 ± 120	29.1 ± 0.6	3.47 ± 0.1	12.3 ± 0.6	12.3	1.2 ± 0.3	1.53	(1)
β Oph	4550 ± 100	46.0 ± 2.5	4.1 ± 0.2	12.2 ± 0.8	13.8	2.90 ± 0.3	2.99	(2)
ε Oph	4850 ± 100	53.5 ± 2.0	5.2 ± 0.1	10.55 ± 0.15	10.2	1.85 ± 0.05	1.91	(3)
ξ Hya	4900 ± 75	92.3 ± 3.0	7.0 ± 0.2	10.4 ± 0.5	9.70	3.04 ± 0.1	3.01	(4)
η Ser	4900 ± 100	125.0 ± 3.0	10.1 ± 0.3	6.3 ± 0.4	6.31	1.60 ± 0.1	1.73	(5)

Notes. The columns R_{mod} and M_{mod} indicate the radius and mass derived from a detailed models, whereas R and M indicate the radius and mass derived from Eqs. (9) and (10).

References. (1) Carrier et al. (2010); A. Miglio, private communication; (2) Kallinger et al. (2010); (3) Kallinger et al. (2008); Mazumdar et al. (2009); Barban et al. (2007); (4) Frandsen et al. (2002); (5) Barban et al. (2004); Hekker et al. (2006); and F. Carrier, private communication; More references on the targets are given in Kallinger et al. (2010).


Fig. 10. $\nu_{\text{max}} - H/B$ relation. Same color code as in Fig. 3.

differs significantly from the 0.7 value found for main-sequence stars and subgiants observed in velocity (Samadi et al. 2007).

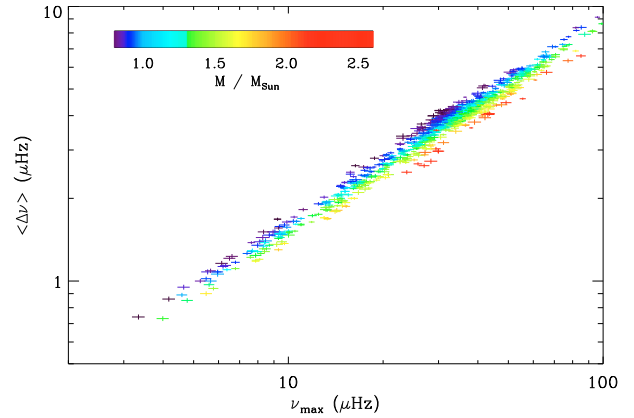
4.4. Height-to-background ratio

Owing to the large variety of stellar activity within the red-giant data set, the ratio H/B does not obey a tight relation, but increases as ν_{max} decreases (Fig. 10). By using the same method as for the amplitude, we derived the relation $H/B \propto \nu_{\text{max}}^{-0.98 \pm 0.05}$. This indicates first that it is possible to measure oscillation with a large height-to-background ratio at very low frequency, which is encouraging for future very long observations as will be provided by Kepler.

The comparison of the mode amplitude and the height-to-background ratio with frequency shows that the mean amplitude of granulation and activity scales as $\nu_{\text{max}}^{-0.36}$. This can be compared to Eq. (7) with an exponent of about -0.85 . If we link the amplitude to the fraction of the convective energy injected in the oscillation, we conclude that this fraction is greater at low frequency. Furthermore, even if less convective energy is injected into the oscillation than into granulation, the fraction injected in the oscillation increases more rapidly at low frequency than the fraction injected into the granulation.

5. Red-giant mass and radius estimate

It is possible to derive the stellar mass and radius from $\langle\Delta\nu\rangle$ and ν_{max} , as done for example by Kallinger et al. (2010) for a few giant targets. This scaling assumes that the mean large separation $\langle\Delta\nu\rangle$ is proportional to the mean stellar density and that ν_{max} varies linearly with the cutoff frequency ν_c , hence with $g/\sqrt{T_{\text{eff}}}$, where g is the surface gravity (Brown et al. 1991). The analysis


Fig. 11. $\nu_{\text{max}} - \langle\Delta\nu\rangle$ relation, restricted to the \mathcal{N}_3 targets. The color code corresponds to the stellar mass derived from Eq. (10).

is extended here to a much larger set of targets, and measurements of higher quality than in Kallinger et al. (2010) because we have introduced the individual stellar effective temperatures.

Before any measurements, we calibrated the scaling relations given below, which provide the stellar mass and radius as a function of the asteroseismic parameters, by comparing the seismic and modeled mass and radius of red giants with already observed solar-like oscillations (Table 3)

$$\frac{R}{R_{\odot}} = r \left(\frac{\nu_{\text{max}}}{\nu_{\text{max},\odot}} \right) \left(\frac{\Delta\nu}{\Delta\nu_{\odot}} \right)^{-2} \left(\frac{T}{T_{\odot}} \right)^{1/2} \quad (9)$$

$$\frac{M}{M_{\odot}} = m \left(\frac{\nu_{\text{max}}}{\nu_{\text{max},\odot}} \right)^3 \left(\frac{\Delta\nu}{\Delta\nu_{\odot}} \right)^{-4} \left(\frac{T}{T_{\odot}} \right)^{3/2} \quad (10)$$

According to the targets summarized in Table 3, the factors r and m are 0.90 ± 0.03 and 0.89 ± 0.07 respectively, for $\Delta\nu_{\odot} = 135.5 \mu\text{Hz}$, $\nu_{\text{max},\odot} = 3050 \mu\text{Hz}$, and $T_{\odot} = 5777 \text{K}$. When taking into account these factors, the agreement between the modeled and seismic values of the radius and mass of the targets listed in Table 3 is better than 7% and agrees within the error bar of the modeling. Calculations were only performed for the \mathcal{N}_3 targets observed with the highest SNR (Fig. 11). The error bars in R and M inferred for the CoRoT red giants from Eqs. (9) and (10) are about 8 and 20%, respectively (Fig. 12).

The equation that indicates the mass is highly degenerate, since $\nu_{\text{max}}^3 \Delta\nu^{-4}$ is nearly constant according to Eq. (3). This degeneracy shows that the temperature strongly impacts the stellar mass. It also indicates that the dispersion about the scaling relation (Eq. (3)) is the signature of the mass dispersion.

Table 4. Scaling with ν_{\max} .

$f(\nu_{\max})$ exponent	$\langle \Delta\nu \rangle$ β	T_{eff} γ	R δ	ν_c α
giants	0.75 ± 0.01	0.04 ± 0.01	-0.48 ± 0.01	1.00 ± 0.02
subgiants ⁽¹⁾	0.71 ± 0.02	-0.02 ± 0.02	-0.58 ± 0.06	0.83 ± 0.10
	$0.77 \pm 0.01^*$			0.97 ± 0.10
dwarfs ⁽²⁾	0.76 ± 0.02	-0.18 ± 0.02	-0.64 ± 0.03	0.97 ± 0.04
	$0.77 \pm 0.01^*$			0.99 ± 0.04

Notes. (*) Value from [Stello et al. \(2009\)](#).

References. (1) [Kallinger et al. \(2010\)](#); [Deheuvels et al. \(2010\)](#); (2) [Kallinger et al. \(2010\)](#); [Mosser et al. \(2008\)](#); [Teixeira et al. \(2009\)](#); [Mathur et al. \(2010a\)](#); [Gaulme et al. \(2010\)](#); J. Ballot, private communication.

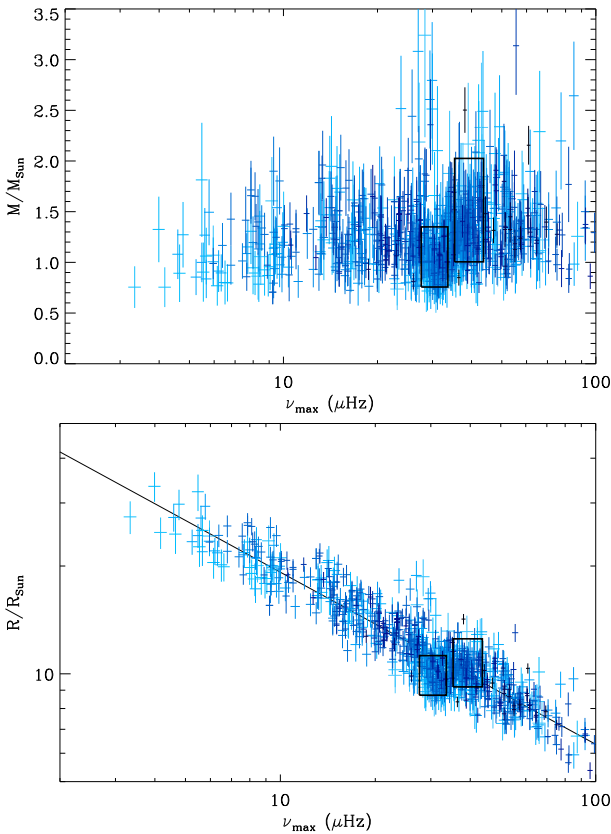


Fig. 12. $\nu_{\max} - M$ and $\nu_{\max} - R$ relations. Same color code as in Fig. 3. The black rectangles delimit the two components of the red clump identified in Figs. 4 and 16.

From Fig. 12, we derive the relation between the stellar radius and ν_{\max} :

$$\frac{R}{R_{\odot}} = (56.7 \pm 1.0) \nu_{\max}^{-0.48 \pm 0.01}. \quad (11)$$

As in previous similar equations, ν_{\max} is expressed in μHz and the error bars are provided conservative.

We analyzed this result to examine the extent to which the exponent close to $-1/2$ is caused by the dependence of the cutoff frequency on the gravity field g and to establish the relation between ν_{\max} and ν_c . To perform both steps in detail and to understand the difference reported in Eq. (3) relative to [Stello et al. \(2009\)](#), we assumed a variation in the cutoff frequency with ν_{\max} of $\nu_c \propto \nu_{\max}^{\alpha}$, and then reapplied Eqs. (9) and (10), taking into

account the scalings $\langle \Delta\nu \rangle \propto \nu_{\max}^{\beta}$ and $T_{\text{eff}} \propto \nu_{\max}^{\gamma}$. We obtained a new relation $R \propto \nu_{\max}^{\delta}$

$$R \propto \nu_{\max}^{\alpha - 2\beta + \gamma/2}, \quad (12)$$

which has to be consistent with (Eq. (11)). Then, when we introduce the numerical values found for the exponents of the different fits, the comparison of Eq. (12) with Eq. (11) gives an exponent α very close to 1, within 2%. This demonstrates that the ratio ν_{\max}/ν_c is constant, which was widely assumed but is verified for the first time for red giants. Its value is about 0.64.

From Table 1 of [Kallinger et al. \(2010\)](#) completed with a few other solar-targets benefiting from a precise modeling (HD 203608, [Mosser et al. 2008](#); ι Hor, [Teixeira et al. 2009](#); HD 52265, Ballot et al., in preparation; HD 170987, [Mathur et al. 2010a](#); HD 46375, [Gaulme et al. 2010](#)), we can derive the exponent α from the values of β , γ , and δ for main-sequence stars and for subgiants. In spite of the quite different set of exponents, we infer in both cases $\alpha \simeq 1$, namely a relation between ν_c and ν_{\max} very close to linear (Table 4). This proves that for all stellar classes the assumption of a fixed ratio ν_{\max}/ν_c is correct. Error bars for subgiants and main-sequence stars are larger than in the red-giant case because of the limited set of stars, and maybe also due to inhomogeneous modeling.

6. Red-giant population

6.1. Red clump

[Miglio et al. \(2009\)](#) compared synthetic, composite stellar populations to CoRoT observations. The analysis of the distribution in ν_{\max} and $\langle \Delta\nu \rangle$ allows them to identify red-clump giants and to estimate the properties of poorly-constrained populations. Benefitting from both the reduction in the error bars and the extension of the analysis to lower frequencies compared to previous works, we can derive precise properties of the red clump (Fig. 14).

The distribution of ν_{\max} is centered around $30.2 \mu\text{Hz}$ with 69% of the values being within the range $30.2 \pm 2.0 \mu\text{Hz}$. The maximum of the distribution of ν_{\max} is located at $29.7 \pm 0.2 \mu\text{Hz}$. The corresponding distribution of $\langle \Delta\nu \rangle$ is centered around $3.96 \mu\text{Hz}$ with 69% of the values being within the range $3.96 \pm 0.33 \mu\text{Hz}$, and its maximum being located at $3.97 \pm 0.03 \mu\text{Hz}$. A second contribution of the red clump can be identified around $40 \mu\text{Hz}$. This feature may correspond to the secondary clump of red-giant stars predicted by [Girardi \(1999\)](#).

Table 5 presents the mean values and the distribution of the physical parameters identified for the peak and the shoulder of the clump stars: the mean values of the radius are comparable for the two components, but the effective temperature, mass,

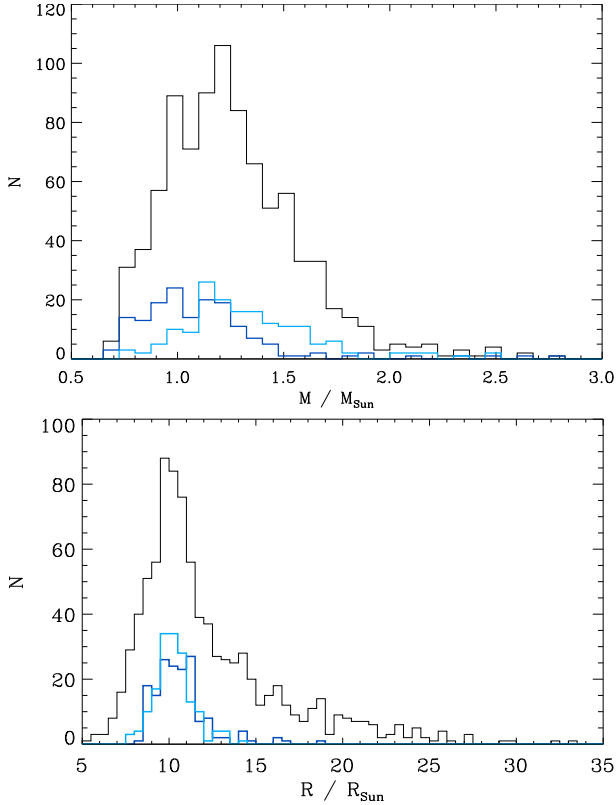


Fig. 13. Histograms of the stellar mass and radius. The curves in dark and light blue correspond, respectively, to the components of the red clump around 30 and 40 μHz . The main difference appears in the mass distribution: 35% higher for the component at 40 μHz . 1- σ uncertainties at the red clump location are typically $0.24 M_{\odot}$ and $0.8 R_{\odot}$, respectively.

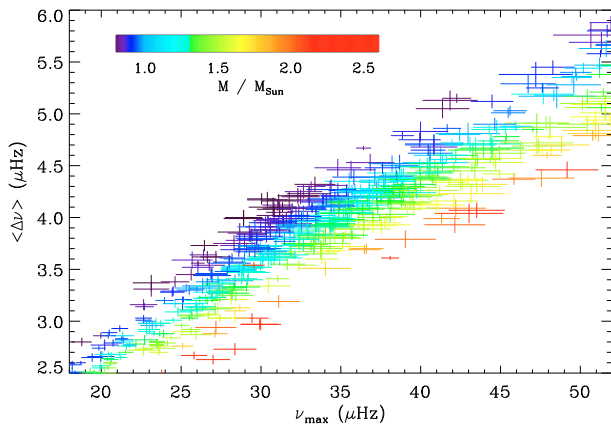


Fig. 14. $\nu_{\text{max}} - \langle \Delta \nu \rangle$ relation around the red clump. Same color code for the mass as in Fig. 11. Low-mass giants are located in the main component of the red clump around 30 μHz .

and luminosity are slightly different. The members of the second component are hotter by about 80 K, brighter, and significantly more massive. The mass distribution disagrees with the theoretical prediction. The distribution is centered on $1.32 M_{\odot}$ (Fig. 13), whereas Girardi (1999) predicts $2-2.5 M_{\odot}$ for solar metallicity. Stars also appear to be brighter, in contrast to theoretical expectations. Figure 14 presents a zoom into the red-clump region of the $\langle \Delta \nu \rangle$ versus ν_{max} relation and shows that stars less massive than $1 M_{\odot}$ are numerous in the main component of the clump but rare in the shoulder. In contrast to Girardi (1999), we do not identify many stars with a mass above $2 M_{\odot}$ near the second

Table 5. Distribution of the red-clump parameters.

Freq. (μHz)	# of stars	R/R_{\odot}	M/M_{\odot}	L/L_{\odot}	T_{eff} (K)
28-32	146	$10.0^{+1.1}_{-1.3}$	$1.00^{+0.19}_{-0.18}$	$38.5^{+9.7}_{-10.0}$	4510^{+170}_{-180}
	LRc01	$10.1^{+0.7}_{-0.7}$	$1.01^{+0.17}_{-0.15}$	$39.0^{+9.5}_{-7.0}$	4530^{+140}_{-150}
	LRA01	$9.8^{+0.7}_{-0.6}$	$0.98^{+0.20}_{-0.12}$	$38.1^{+8.5}_{-7.0}$	4480^{+120}_{-100}
37-43	137	$10.3^{+1.1}_{-0.7}$	$1.34^{+0.25}_{-0.18}$	$42.4^{+11.2}_{-8.3}$	4580^{+140}_{-170}
	LRc01	$10.3^{+0.8}_{-0.7}$	$1.33^{+0.22}_{-0.15}$	$42.1^{+9.4}_{-7.8}$	4580^{+130}_{-140}
	LRA01	$10.4^{+1.2}_{-0.6}$	$1.36^{+0.28}_{-0.19}$	$42.7^{+8.3}_{-7.3}$	4590^{+120}_{-150}

Notes. The 2nd column gives first the total number of targets considered in each region of the clump, then indicates which field is considered. The following columns present the main values of the stellar parameters and the dispersion in their distribution in each region.

component of the clump. Selecting stars in the secondary component of the clump by adopting only a criterion on ν_{max} is certainly insufficient, since many stars with ν_{max} around 40 μHz can belong to the tail of the distribution of the main component. The discrepancy with the prediction of Girardi (1999) may result from the way that we identify the stars and a refined identification will be necessary to describe this secondary component more accurately.

Figure 15 presents an HR diagram of the red-clump stars among all targets with precise asteroseismic parameters, the stellar luminosity being derived from the Stefan-Boltzmann law. We note a mass gradient in the direction of hot and luminous objects. However, we note that the members of the two components are intricately mixed in this diagram.

6.2. Comparison center/antcenter

We compared the distribution of ν_{max} and $\langle \Delta \nu \rangle$ in the 2 CoRoT runs LRc01 and LRA01. The LRc01 run, centered on $(\alpha, \delta) = (19^{\text{h}}25^{\text{m}}, 0^{\circ}30')$, targets an inner region of the Galaxy of Galactic longitude and latitude 37° and $-07^{\circ}45'$, respectively, 38° away from the Galactic center. Targets of the run LRA01 are located in the opposite direction of LRc01, centered on $(\alpha, \delta) = (6^{\text{h}}42^{\text{m}}, -0^{\circ}30')$, of lower Galactic latitude ($-01^{\circ}45'$) and Galactic longitude of 212° . According to the reddening inferred for the targets, a typical 13th magnitude red giant of the red clump is located at 3 kpc.

The histograms of ν_{max} and $\langle \Delta \nu \rangle$ for both fields are compared in Fig. 16. They show comparable relative values in all frequency ranges except for the location of the clump stars. The main component of the red clump is much less pronounced in LRA01 than LRc01; on the other hand, the second component of the clump is more populated in LRA01. The distribution concerning LRA01, with two components, strongly supports the identification of the secondary clump. Since the two populations were selected on the basis of homogeneous criteria and show comparable scaling laws for all asteroseismic parameters, understanding the difference between them will require additional analysis taking into account more parameters than those given by asteroseismology, to investigate the roles of evolutionary status, metallicity, and position in the Galaxy.

7. Conclusion

We have demonstrated that it is possible to extract statistical information from the high-precision photometric time series of a

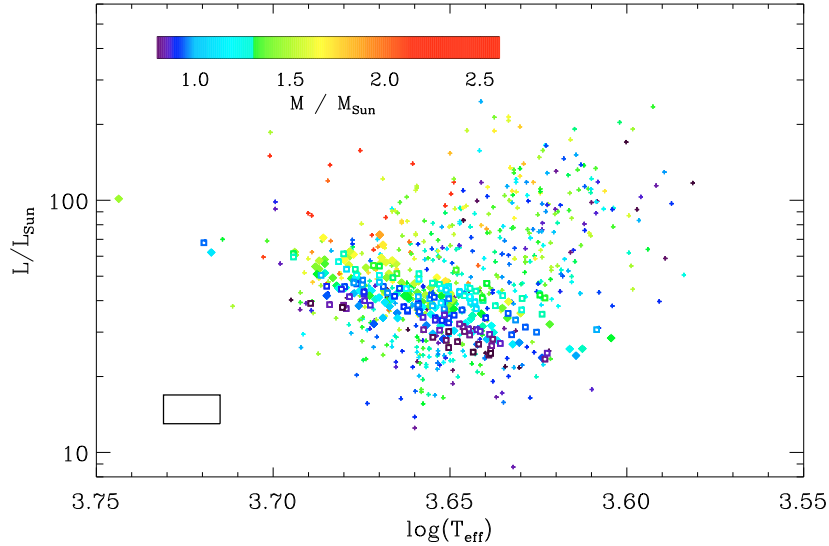


Fig. 15. HR diagram of the N_3 targets of LRa01 and LRC01. The estimates of the mass are derived from Eq. (10) and are presented with the same color code as Fig. 11. For clarity, individual bars are not represented. The mean $1\text{-}\sigma$ error box is given in the lower-left corner of the diagram. Cross are replaced by open squares for stars in the main component of the red clump, and diamonds for the second component.

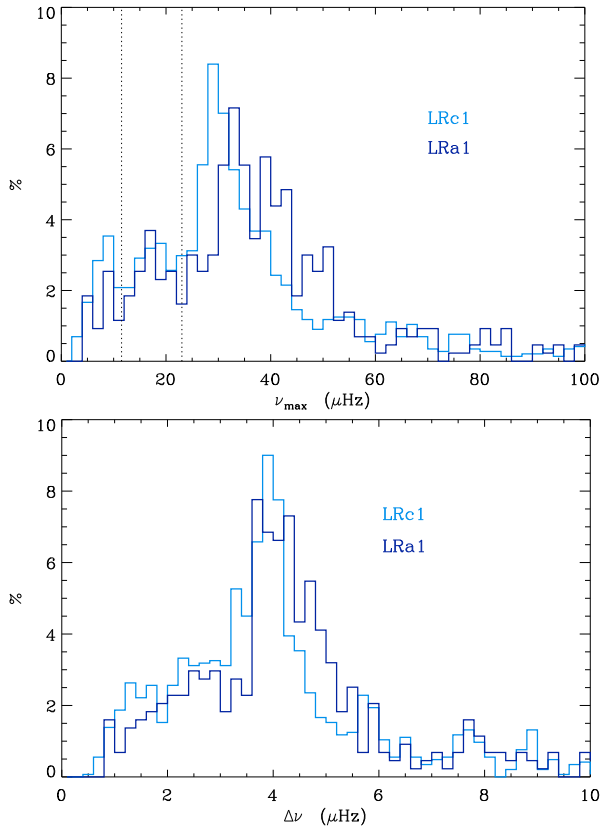


Fig. 16. Histograms of ν_{\max} and $\langle \Delta \nu \rangle$, comparing the populations in LRC01 and LRA01. The secondary red-clump signature is mainly due to the population in LRA01. $1\text{-}\sigma$ uncertainties at the red clump are typically $0.06\ \mu\text{Hz}$ for the $\langle \Delta \nu \rangle$ -axis, $1.0\ \mu\text{Hz}$ for the ν_{\max} -axis, and 1% on both y -axes. As in Fig. 4, the dotted lines in the histogram of ν_{\max} indicate the deficits of reliable results around 11.6 and $23.2\ \mu\text{Hz}$.

large sample of red giants observed with CoRoT and analyzed with an automated asteroseismic pipeline. We summarize here the main results of our study and the remaining open issues:

- Out of more than 4600 time series, we have identified more than 1800 red giants exhibiting solar-like oscillations. We

have extracted a full set of precise asteroseismic parameters for more than 900 targets.

- Thanks to our detection method, we have been able to observe precisely large separations as small as $0.75\ \mu\text{Hz}$. We have obtained reliable information about the seismic parameters $\langle \Delta \nu \rangle$ and ν_{\max} for ν_{\max} in the range $[3.5, 100\ \mu\text{Hz}]$. We have shown that the detection and measurement method does not introduce any bias for ν_{\max} above $6\ \mu\text{Hz}$. This allows us to study in detail the red clump in the range $[30, 40\ \mu\text{Hz}]$.
- We have proposed scaling relations for the parameters defining the envelope where the asteroseismic power is observed in excess. We note that the relation defining the full-width at half-maximum $\delta\nu_{\text{env}}$ of the envelope cannot be extended to solar-like stars. The scaling relation between $\delta\nu_{\text{env}}$ and ν_{\max} is definitely not linear, being $\delta\nu_{\text{env}} \propto \nu_{\max}^{0.90}$. The maximum amplitude scales as $\nu_{\max}^{-0.85}$ or $(L/M)^{0.89}$. Deriving bolometric amplitudes will require more work, including examination of the equipartition of energy between the modes and stellar atmosphere modeling.
- When complemented with effective temperature, asteroseismic parameters $\langle \Delta \nu \rangle$ and ν_{\max} can be used to determine the stellar mass and radius. Red-giant masses derived from asteroseismology are degenerate, but their value can be estimated with a typical uncertainty of about 20%. We have established a tight relation between the maximum amplitude frequency ν_{\max} and the red-giant radius from an unbiased analysis in the range $[7\text{--}30 R_{\odot}]$, which encompasses the red-clump stars. This relation scales as $R_{\text{RG}} \propto \nu_{\max}^{-0.48}$.
- From this result, and taking into account the scaling law $\langle \Delta \nu \rangle \propto \nu_{\max}^{0.75}$, we have shown that the ratio ν_{\max}/ν_c is constant for giants. A similar analysis performed on main-sequence stars and subgiants reaches the same result: ν_{\max}/ν_c is also nearly constant.
- As a by-product, we have shown that scaling laws are slightly but undoubtedly different for giants, subgiants and dwarfs. For red-giant stars only, that the temperature is nearly a degenerate parameter plays a significant role. As a consequence, global fits encompassing *all* stars with solar-like oscillations may not be precise, since they do not account for the different physical conditions between main-sequence and giant stars.

- The comparison of data from 2 runs pointing in different directions at different Galactic latitudes has shown that the stellar properties are similar; the dispersion about the global fits is too small to be detectable. The main difference between the 2 runs is their different stellar populations. The distributions of the asteroseismic parameters are globally similar, except for the location of the red clump.
- We have obtained precise information about the red-clump stars. Statistical asteroseismology makes it possible to identify the expected secondary clump and to measure the distribution of the fundamental parameters of the red-clump stars. We have shown that the relative importance of the two components of the clump is linked to the stellar population. The precise determination of the red-clump parameters will benefit from the asteroseismic analysis and the modeling of individual members of the clump.

These points demonstrate the huge potential of asteroseismology for stellar physics.

Acknowledgements. This work was supported by the Centre National d'Études Spatiales (CNES). It is based on observations with CoRoT. The research has made use of the Exo-Dat database, operated at LAM-OAMP, Marseille, France, on behalf of the CoRoT/Exoplanet program. TM acknowledges financial support from Belpo for contract PRODEX-GAIA DPAC.

The work of K.B. was supported through a postdoctoral fellowship from the "Subside fédéral pour la recherche 2010", Université de Liège. S.H. acknowledges support by the UK Science and Technology Facilities Council. The research leading to these results has received funding from the European Research Council under the European Community's Seventh Framework Programme (FP7/2007–2013)/ERC grant agreement n°227224 (PROSPERITY), as well as from the Research Council of K.U.Leuven grant agreement GOA/2008/04.

References

Alonso, A., Arribas, S., & Martínez-Roger, C. 1999, *A&AS*, 140, 261
 Appourchaux, T. 2004, *A&A*, 428, 1039
 Appourchaux, T., Michel, E., Auvergne, M., et al. 2008, *A&A*, 488, 705
 Auvergne, M., Bodin, P., Boissard, L., et al. 2009, *A&A*, 506, 411

Barban, C., De Ridder, J., Mazumdar, A., et al. 2004, in *SOHO 14 Helio- and Asteroseismology: Towards a Golden Future*, ed. D. Danesy, ESA SP, 559, 113
 Barban, C., Matthews, J. M., De Ridder, J., et al. 2007, *A&A*, 468, 1033
 Barban, C., Deheuvels, S., Baudin, F., et al. 2009, *A&A*, 506, 51
 Baudin, F., Barban, C., Belkacem, K., et al. 2010, *A&A*, submitted
 Bedding, T., Huber, D., Stello, D., et al. 2010, *ApJ*, 713, L176
 Benomar, O., Baudin, F., Campante, T. L., et al. 2009, *A&A*, 507, L13
 Brown, T. M., Gilliland, R. L., Noyes, R. W., & Ramsey, L. W. 1991, *ApJ*, 368, 599
 Carrier, F., De Ridder, J., Baudin, F., et al. 2010, *A&A*, 509, A73
 De Ridder, J., Barban, C., Baudin, F., et al. 2009, *Nature*, 459, 398
 Deheuvels, S., Bruntt, H., Michel, E., et al. 2010, *A&A*, 515, A87
 Deleuil, M., Meunier, J. C., Moutou, C., et al. 2009, *AJ*, 138, 649
 Dobashi, K., Uehara, H., Kandori, R., et al. 2005, *PASJ*, 57, S1
 Dupret, M., Belkacem, K., Samadi, R., et al. 2009, *A&A*, 506, 57
 Frandsen, S., Carrier, F., Aerts, C., et al. 2002, *A&A*, 394, L5
 García, R. A., Régulo, C., Samadi, R., et al. 2009, *A&A*, 506, 41
 Gaulme, P., Deheuvels, S., Weiss, W. W., et al. 2010, *A&A*, submitted
 Girardi, L. 1999, *MNRAS*, 308, 818
 Hekker, S., Aerts, C., De Ridder, J., & Carrier, F. 2006, *A&A*, 458, 931
 Hekker, S., Kallinger, T., Baudin, F., et al. 2009, *A&A*, 506, 465
 Huber, D., Stello, D., Bedding, T. R., et al. 2009, *Commun. Asteroseismol.*, 160, 74
 Kallinger, T., Guenther, D. B., Matthews, J. M., et al. 2008, *A&A*, 478, 497
 Kallinger, T., Weiss, W. W., Barban, C., et al. 2010, *A&A*, 509, A77
 Kjeldsen, H., & Bedding, T. R. 1995, *A&A*, 293, 87
 Mathur, S., Garcia, R., Catala, C., et al. 2010a, *A&A*, accepted
 Mathur, S., García, R. A., Régulo, C., et al. 2010b, *A&A*, 511, A46
 Mazumdar, A., Mérand, A., Demarque, P., et al. 2009, *A&A*, 503, 521
 Michel, E., Samadi, R., Baudin, F., et al. 2009, *A&A*, 495, 979
 Miglio, A., Montalbán, J., Baudin, F., et al. 2009, *A&A*, 503, L21
 Mosser, B., & Appourchaux, T. 2009, *A&A*, 508, 877
 Mosser, B., & Appourchaux, T. 2010, in *New insights into the Sun*, ed. M. Cunha, & M. Monteiro, in press
 Mosser, B., Bouchy, F., Catala, C., et al. 2005, *A&A*, 431, L13
 Mosser, B., Deheuvels, S., Michel, E., et al. 2008, *A&A*, 488, 635
 Mosser, B., Michel, E., Appourchaux, T., et al. 2009, *A&A*, 506, 33
 Rowles, J., & Froebrich, D. 2009, *MNRAS*, 395, 1640
 Roxburgh, I. W., & Vorontsov, S. V. 2006, *MNRAS*, 369, 1491
 Samadi, R., Georgobiani, D., Trampedach, R., et al. 2007, *A&A*, 463, 297
 Stello, D., Chaplin, W. J., Basu, S., Elsworth, Y., & Bedding, T. R. 2009, *MNRAS*, 400, L80
 Stello, D., Basu, S., Bruntt, H., Mosser, B., & Stevens, I. 2010, *ApJ*, 713, L182
 Teixeira, T. C., Kjeldsen, H., Bedding, T. R., et al. 2009, *A&A*, 494, 237